Letter

Elucidation of the electron transfer mechanism in Eu^{2+} and Sm^{3+} codoped CaF_2: A step towards better understanding of trapping and detrapping in luminescent materials

Jonas J. Joos [1,*] David Van der Heggen [1] Lucia Amidani [2,†] Luis Seijo [3] and Zoila Barandiarán [3]

[1] *LumiLab, Department of Solid State Sciences and Center for Nano- and Biophotonics (NB-Photonics), Ghent University, 9000 Ghent, Belgium*

[2] *European Synchrotron Radiation Facility (ESRF), 38000 Grenoble, France*

[3] *Departamento de Química, Instituto Universitario de Ciencia de Materiales Nicolás Cabrera, and Condensed Matter Physics Center (IFIMAC), Universidad Autónoma de Madrid, 28049 Madrid, Spain*

(Received 4 August 2021; revised 20 October 2021; accepted 25 October 2021; published 16 November 2021)

Many-electron multiconfigurational *ab initio* calculations are combined with x-ray spectroscopy to scrutinize a popular model for electron transfer in lanthanide-doped crystals which hypothesizes that the electrons are conveyed by the conduction band of the host. Contrary to this accepted picture, our combined theoretical-experimental effort shows that the reversible electron phototransfer from Eu^{2+} to Sm^{3+} in CaF_2 is direct, from metal to metal. It is theoretically predicted and experimentally verified that visible light induces the reverse electron transfer.

DOI: 10.1103/PhysRevB.104.L201108

The first evidence of a photoinduced electron transfer reaction from a divalent to a trivalent lanthanide in CaF_2 crystals was reported by Feofilov in very diluted Eu and Sm codoped samples exposed to x rays [1]. Shortly after, Welber showed that the phototransfer is reversible and that it can be triggered in both directions with ultraviolet (UV) light:

$$Eu^{2+} + Sm^{3+} \underset{h\nu_2}{\overset{h\nu_1}{\rightleftharpoons}} Eu^{3+} + Sm^{2+}, \tag{1}$$

with $\lambda_1 = 255$ nm, and $\lambda_2 = 310$ nm [2]. Photoinduced reversible electron transfer had earlier been reported by Keller *et al.* [3,4] in so-called infrared (IR) stimulable phosphors: SrS:Ce,Sm,

$$Ce^{3+} + Sm^{3+} \underset{h\nu_2}{\overset{h\nu_1}{\rightleftharpoons}} Ce^{4+} + Sm^{2+}, \tag{2}$$

and SrS:Eu,Sm [Eq. (1)], with $h\nu_1$ in the UV and $h\nu_2$ in the IR.

The significance of the reversible photoreactions (1) and (2) is broadly recognized as this mechanism allows for a controllable energy storage (upon the forward reaction) and release (upon the backward reaction) [5–7]. If the backtransfer results into light emission, it is called optically stimulated luminescence (OSL). Alternatively the backtransfer can be provoked by increasing the temperature in which case the process is called thermoluminescence [8].

OSL enables luminescence dosimetry [9–12] or medical imaging [13–18]. In these cases, IR or red light induces the OSL, having a sufficiently low photon energy to avoid the direct excitation of nonoxidized donors. If the OSL wavelength is shorter, a competition between nonoxidized donors and reduced acceptors (filled traps) can emerge, effectively limiting the performance of current state-of-the-art persistent phosphors [19,20]. Many more technological applications rely on electron transfer processes among dopants or with other crystallographic defects [21–24]. At the same time, electron transfer processes are known to limit the performance of luminescent materials when multiple valences coexist or when high excitation intensities are used [25–30]. This demonstrates that an in-depth understanding of the electron transfer is essential in developing the next generation luminescent materials, allowing one to amplify the functional behavior while suppressing the associated disadvantages.

The basics of the mechanism of such reversible electron transfers were proposed in the pioneering reports we have just referred to [2–4]. Mixed energy schemes, combining many-electron energy levels of activators with one-electron energy levels of hosts, were the theoretical framework used to incorporate experimental data and build a rationale of the whole process. Accordingly, in the CaF_2:Eu,Sm case [Eq. (1)], upon irradiation with $h\nu_1$ light, electrons are assumed to be excited from the Eu^{2+} activator to the CaF_2 conduction band (CB) and trapped later by the Sm^{3+} activator; luminescence from the resulting Sm^{2+} can be detected and, ultimately, energy is stored in metastable Sm^{2+} centers. Further irradiation with $h\nu_2$ excites the trapped electrons from Sm^{2+} back to Eu^{3+} through the CB; the backtransferred electrons are then captured in an excited state of Eu^{2+}, which finally decays radiatively.

Adaptations of this original mechanism have repeatedly been proposed in order to account for experimental data in other hosts and activator pairs [7,15,31–35]. Yet, the central hypothesis of the mechanism has not been altered: the forward and backward electron transfers are conveyed by the

*jonas.joos@ugent.be

†Present address: Helmholtz-Zentrum Dresden-Rossendorf, 01314 Dresden, Germany.

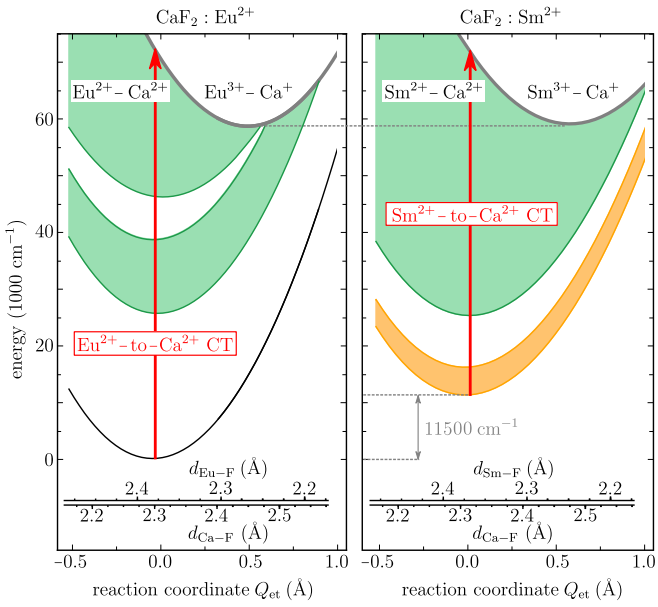

FIG. 1. MMCT many-electron energy diagrams of Eu^{2+}/Ca^{2+} (left) and Sm^{2+}/Ca^{2+} (right) pairs in CaF_2. Upward arrows: direct, photoinduced, vertical dopant-to-host charge transfer. Very dense energy regions of pair states are indicated with color fills: black/orange: Eu/Sm $4f^N$-Ca^{2+}; green: Eu/Sm $4f^{N-1}5d$-Ca^{2+}; gray: lowest state of Eu^{3+}-Ca^+ (left) and Sm^{3+}-Ca^+ (right). The Sm^{2+}-Ca^{2+} diagram is shifted +11 500 cm^{-1} so that the lowest local host energy level of both diagrams coincide. The shift corresponds to the difference between the minimum-to-minimum ionization potential of Eu^{2+} in CaF_2 (15 300 cm^{-1}) and that of Sm^{2+} in CaF_2 (3800 cm^{-1}).

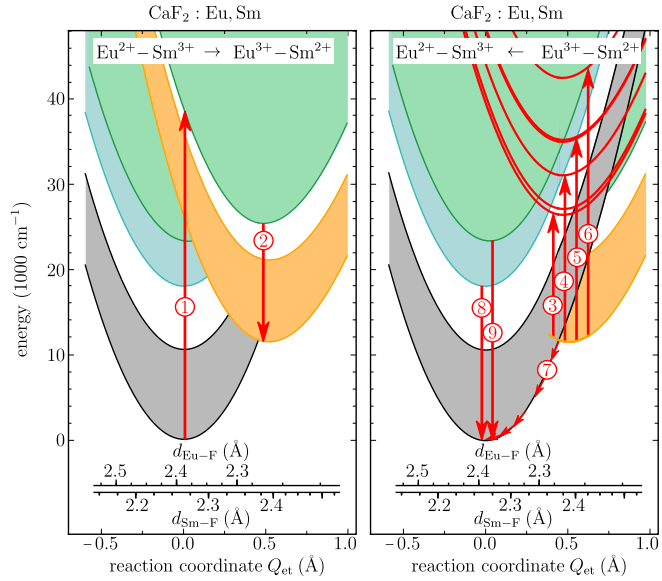

FIG. 2. The calculated MMCT many-electron energy diagram of Eu^{2+}/Sm^{3+} pairs in CaF_2 is plotted in the left and right graphs with different emphases to better visualize the forward and backward electron transfers of Eq. (1). In each case, pair states resulting from the electron transfer are plotted in the foreground. Left: forward, photoinduced Eu^{2+}-to-Sm^{3+} electron transfer (1), followed by Sm^{2+} $4f^5 5d e_g^1$-$4f^6$ emission (2). Right: backwards, Sm^{2+}-to-Eu^{3+} electron transfer; photoinduced through Sm^{2+} absorptions in the visible (3, 4, 5) and in the UV (6) and thermally induced (7). OSL resulting from Sm^{3+} $^4G_{5/2}(19\ \Gamma_{8u})$ (8) or Eu^{2+} $4f^6 5d^1$-$4f^7$ (9) emissions. Very dense energy regions of pair states are indicated with color fills: gray, turquoise, and green for Eu^{2+}-Sm^{3+} $4f^7(^8S)$-$4f^6(^6H/^6F)$, $4f^7(^8S)$-$4f^6(^4L)$, and $4f^6 5d^1$-$4f^6$ pair states; orange and green for Eu^{3+}-Sm^{2+} $4f^6$-$4f^6$, and $4f^6$-$4f^5 5d^1$ pair states. The Eu^{3+}-Sm^{2+} ground state minimum is 11 500 cm^{-1} above the Eu^{2+}-Sm^{3+} minimum.

conduction band of the host, i.e., by delocalization of the transferred electron.

In this work we investigate whether the phototransfer in CaF_2:Eu,Sm is bridged by the CB of the host or whether it is a direct reversible Eu^{2+}/Sm^{3+} metal-to-metal charge transfer (MMCT). Many-electron theoretical methods are applied to both the dopants and the host, so that dopant-to-host and dopant-to-dopant charge transfer energies are unambiguously comparable.

Configurational coordinate diagrams for the electron transfer between dopant (Eu and Sm) and host (Ca) cations are diabatically calculated from the potential energy surfaces of individual embedded clusters [36–40], as obtained with state-of-the-art multiconfigurational multireference correlated wave function quantum chemical methods [41–69]. Details of the methods and intermediate results are given in the Supplemental Material (SM) [70].

The vertical phototransfer of an electron from the Eu^{2+} activator to the CaF_2 host is visualized in the left panel of Fig. 1 by the upward arrow originating from the Eu^{2+}-Ca^{2+} pair ground state. An excitation energy of $h\nu_1^{calc} \geqslant$ 73 400 cm^{-1} ($\leqslant$136 nm) is required to transfer a $4f$ electron from the Eu^{2+} $4f^7$ ground state to the lowest empty $3d$ shell of a nearest Ca^{2+} host ion (note that we are using here an approximate one-electron language, although the calculated energies are between many-electron states). This large energy is not surprising given the thermodynamically very low tendency of Ca^{2+} to become reduced to a monovalent oxidation state. However, Welber found that a much smaller excitation energy induces the forward electron transfer: $h\nu_1 = 39\,216$ cm^{-1} (255 nm) [2]. Additionally, it was found that the electron backtransfer, Sm^{2+}-to-Eu^{3+}, was induced with $h\nu_2 = 32\,258$ cm^{-1} (310 nm) [2]; this is a much lower value than the lowest Sm^{2+}-to-Ca^{2+} CT we find in the *ab initio* Sm^{2+}/Ca^{2+} MMCT calculations: $h\nu_2^{calc} \geqslant 61\,500$ cm^{-1} ($\leqslant$162 nm) (upward arrow in Fig. 1, right).

From these very large discrepancies between measured and calculated values we can conclude that the central hypothesis, i.e., that the CaF_2:Eu,Sm reversible electron transfer is conveyed by the CB, is not supported by theory.

Therefore we focused on finding the mechanism of the reversible electron transfer using a combined theoretical and experimental approach. The outcome is that the reversible electron transfer between Eu and Sm involves direct excitations to MMCT pair states, which corresponds to a local model of electron transfer.

The excitation energy that was found to induce the forward Eu^{2+}-to-Sm^{3+} electron transfer, $h\nu_1 = 39\,216$ cm^{-1} (255 nm) [2], is plotted as arrow 1 in the calculated Eu^{2+}/Sm^{3+} MMCT energy diagram of Fig. 2, originating from the $Eu^{2+}(4f^7)$-$Sm^{3+}(4f^6)$ ground state. This energy

does not produce intra-Eu^{2+} excitation [69], but it is sufficient to reach structurally stressed levels within the crowded $Eu^{3+}(4f^6)$-$Sm^{2+}(4f^55d)$ manifold (green). Interestingly, it is only slightly higher than the calculated threshold for MMCT excitation producing Eu^{2+} $4f \rightarrow Sm^{3+}$ $5d$ electron transfer: $h\nu_1^{\text{calc}} \geqslant 38\ 700\ \text{cm}^{-1}$ ($\leqslant$258 nm). After excitation, nonradiative relaxation leads to the bottom of the $Eu^{3+}(4f^6)$-$Sm^{2+}(4f^55d)$ manifold (green) from where the Sm^{2+} lowest electric dipole allowed d-f emission, $1A_{1u} \rightarrow 1T_{1g}$, is calculated to be at 13 611 cm^{-1} (735 nm) (arrow 2; cf. Supplemental Material Table S4). For the CaF_2 host, the dense $4f^55d^1$ manifold (starting at 13 855 cm^{-1}) of the Sm^{2+} dopant completely overlaps with the $4f^6(^5D_J)$ ($J = 0$–3) levels (starting at 16 497 cm^{-1}; see also Table S4 and Fig. S6), so only interconfigurational $5d$-$4f$ emission and no competition with intraconfigurational $4f$-$4f$ emission, which is known to occur in various other crystals [71–73], is expected. Indeed, Welber probed the forward electron transfer by observing the intensity of this Sm^{2+} $5d$-$4f$ emission, whose zero-phonon line is experimentally found at 708.5 nm (14 114 cm^{-1}) in CaF_2 [2,74].

The close agreement between experiment and theory for the MMCT excitation and for the subsequent Sm^{2+} d-f emission suggests that the forward phototransfer is a direct Eu^{2+}-to-Sm^{3+} MMCT that leaves the resulting Sm^{2+} ready to emit in the red.

Feofilov and Welber showed that x rays induce the same forward transfer without compromising the reversibility of the process [1,2].

The backwards phototransfer observed by Welber at $h\nu_2 =$ 31 949 cm^{-1} (313 nm) [2], can be found in Fig. 2 (right) represented by arrow 6. (The origin of arrow 6 is at the Eu^{3+}-Sm^{2+} ground state minimum, which is 11 500 cm^{-1} above the Eu^{2+}-Sm^{3+} minimum.) This transition corresponds to a direct MMCT absorption where one of the electrons from the Sm^{2+} $4f^6$ shell is transferred to the Eu^{3+} center, forming an Eu^{2+} ion in a $4f^65d^1$ excited state which is ready to emit.

Next to direct MMCT absorptions from the lowest metastable Eu^{3+}-Sm^{2+} state, also interconfigurational $4f^6$-$4f^55d^1$ transitions within the Sm^{2+} ion can induce electron backtransfer. Figure 3 shows the Sm^{2+} absorption spectrum in the visible range, as originally measured by Loh, compared to the spectrum obtained from our *ab initio* calculations (see also SM [70,75–79]). Allowed electric dipole absorptions correspond to $Sm^{2+}4f^6(1A_{1g}) \rightarrow 4f^55d^1(nT_{1u})$ transitions according to the selection rules for the O_h point group. The most dominant bands are situated in the red (arrow 3) and violet (arrow 5) spectral regions. A less intense absorption band is found in the green (arrow 4) region. More details can be found in the SM, including the calculated relative oscillator strengths [70].

Upon absorption of violet light (arrow 5), relaxation by intersystem crossing from the excited Eu^{3+}-$Sm^{2+}4f^6$-$4f^55d^1$ to the dense Eu^{2+}-$Sm^{3+}4f^65d^1$-$4f^5$ manifold is possible without the need to overcome a thermal barrier, i.e., electron transfer is expected. In contrast, upon red or green absorption (arrows 3 and 4), intersystem crossing is only possible provided that the associated energy barriers, formed by the crossings between the excited Eu^{3+}-$Sm^{2+}4f^6$-$4f^55d^1$ and

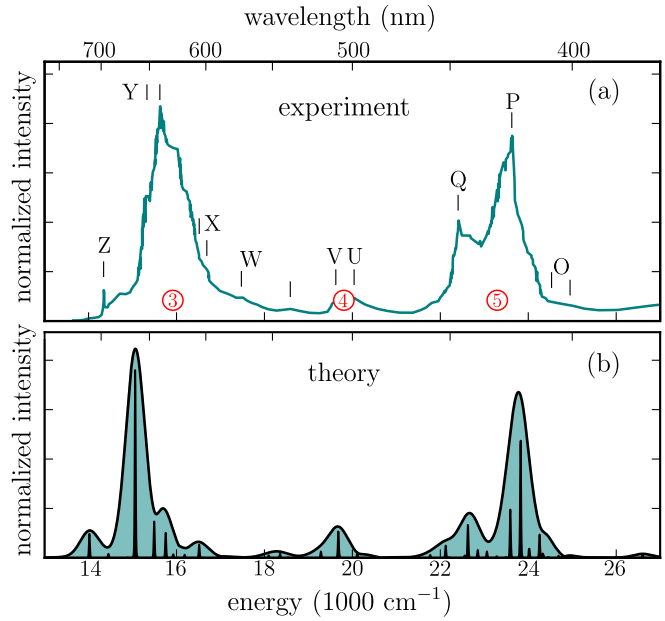

FIG. 3. Lowest $4f^6 \rightarrow 4f^55de_g^1$ absorption bands of Sm^{2+} in CaF_2. Top: experimental, adapted from Loh [75]. Bottom: From *ab initio* multiconfigurational, spin-orbit calculations (this work). The numbers 3,4,5 correspond to the arrows in Fig. 2 (cf. Supplemental Material Tables S4 and S5 and Fig. S7 [70]).

Eu^{2+}-Sm^{3+} levels are overcome. The likelihood for electron transfer is hence much lower in this case.

In the following, the predicted possibility to trigger the backtransfer using a violet LED is verified via an x-ray spectroscopy experiment with simultaneous LED illumination.

In our experiments with CaF_2:1%Eu,0.6%Sm powders, the valence state changes that Eu and Sm undergo, following x-ray and violet light stimulation, are derived from Eu and Sm L_{III} edge high energy resolution fluorescence detected x-ray absorption near edge structure (HERFD-XANES) spectra [Fig. 4(a)] and from radio- (RL) and photoluminescence (PL) spectra, simultaneously recorded with the x-ray spectra [Fig. 4(b)]. Experimental details can be found in the SM [70] and in Refs. [80–85].

During the first 10 minutes (gray shaded area), HERFD-XANES spectra are collected, causing a continuous irradiation of the sample by x rays. The x-ray and RL spectra show that this causes the oxidation of Eu^{2+} and the simultaneous reduction of Sm^{3+}. Quantitative analysis of the x-ray spectra shows that the amounts of oxidized Eu^{2+} and reduced Sm^{3+} are the same within the experimental uncertainty, i.e., about 1.5% of the present Eu and Sm. After 10 minutes, the trend levels off. Then the x-ray irradiation is ceased, leaving the sample to be illuminated by the LED only. The measured PL [Fig. 4(b)] indicates that the LED illumination has the opposite effect as the x-ray irradiation, i.e., a reoxidation of the Sm^{2+} ions that were formed during the 10 minutes of prior x-ray irradiation. Note that OSL associated to the backtransfer (arrows 8 and 9 in Fig. 2) has a negligible intensity compared to the PL that is measured here. The reoxidation of Sm^{2+} and the associated reduction

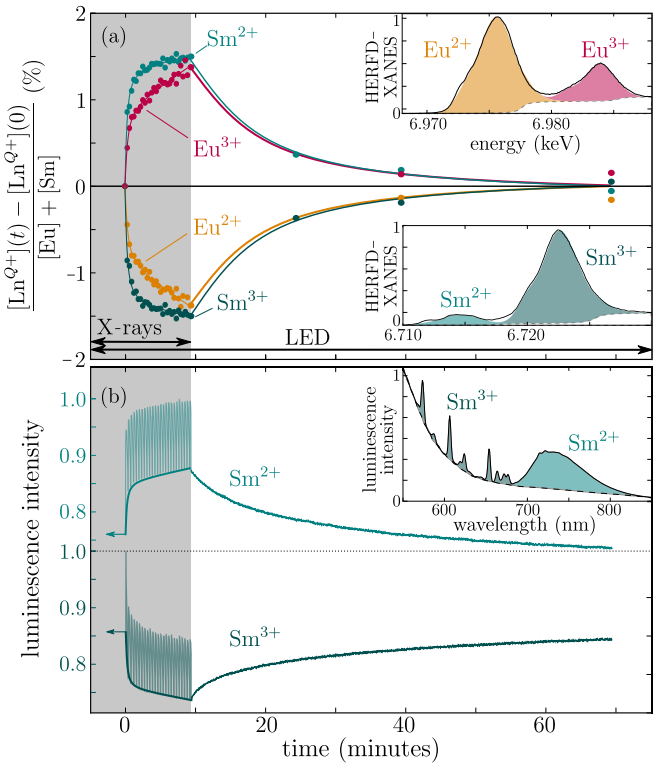

FIG. 4. X-ray (gray shaded area) and light-induced (420 nm) electron transfer in CaF_2:1%Eu,0.6%Sm. (a) The change in oxidation states of Eu and Sm as obtained from HERFD-XANES. The insets display the initial HERFD-XANES spectra at the Eu and Sm L_{III} edges. The colored area is obtained from a fit (see SM [70]) and is used to obtain the transient data points. The curves are plotted as a guide to the eye and were obtained by fitting the available data points. (b) The corresponding response in relative luminescence intensity. The wiggles in the RL signal are due to variations in x-ray intensity during the measurement of consecutive HERFD-XANES spectra. The bold line represents the total PL intensity (i.e., without the contribution of RL during the first 10 minutes), obtained by fitting the available data points. The inset shows the initial PL/RL spectrum and how it was integrated to obtain the transient curves. This experiment was performed at room temperature.

of Eu^{3+} was verified by single HERFD-XANES scans after 15, 30, or 60 minutes of illumination [Fig. 4(a)].

The experiments hence show that violet light has the opposite effect of the x rays on the Eu and Sm oxidation states:

$$Eu^{2+} + Sm^{3+} \underset{\text{violet light}}{\overset{\text{x ray}}{\rightleftharpoons}} Eu^{3+} + Sm^{2+}. \qquad (3)$$

After 60 minutes, the valence changes caused by the x rays were completely reversed by illumination with the violet LED. Multiple subsequent experimental runs were performed, verifying that this effect is reproducible. Importantly, it was verified that no spontaneous backtransfer took place in the absence of illumination, i.e., the backtransfer is solely caused by the visible light.

Although this work is focused on the photoinduced reversible electron transfer at room temperature, it has been long known [1] that after x-ray exposure, the Eu and Sm doped crystals can be bleached to their original state by heating to 700 °C. The calculated MMCT many-electron energy diagram of Fig. 2 (right) suggests the Eu^{3+}-Sm^{2+} ground state is metastable; it shows the thermal backtransfer (arrow heads 7) through an energy barrier whose absolute value (184 cm^{-1}) should be affected by the diabatic approximation. Furthermore, thermally assisted OSL is expected upon red or green stimulation (arrows 3 and 4). This will be the topic of further research.

In summary, we have compared calculated dopant-to-host and dopant-to-dopant electron transfer energies in CaF_2:Eu,Sm with available experimental data to investigate whether the reversible electron transfer between Eu^{2+} and Sm^{3+} is conveyed by the conduction band of the host or by metal-to-metal charge transfer states. We find that (i) the phototransfers to the host are much higher in energy than the experimentally found transition energies and (ii) the calculated metal-to-metal charge transfer energies match experimental data. The comparisons are meaningful because the same many-electron theoretical methods were applied to the dopants and host electronic structure. These results challenge the usual hypothesis that the conduction band of the host mediates the energy storage and detrapping processes in this and similar materials. Moreover, we present experimental evidence that the backtransfer can be induced at room temperature with violet light, which suggests the CaF_2:Eu,Sm material can be used in, e.g., dosimetry. This new evidence is difficult to reconcile with the CB hypothesis; however, the many-electron MMCT methods used here not only predict but also describe the mechanism of the optically stimulated process in the visible spectral range. The abundance of electron transfer processes in functional materials for numerous applications points out the importance of advancing experimental evidence and theoretical insight at once.

J.J.J. and D.V.d.H. acknowledge the UGent Special Research Fund (BOF/PDO/2017/ 002101 and BOF16/DOC/327). This work was partially supported by Ministerio de Economía y Competitividad, Spain (Dirección General de Investigación y Gestión del Plan Nacional de I + D + i, MAT2017-83553-P). We acknowledge the Fund for financial support for a travel grant (Grant No. V416818N) and the European Synchrotron Radiation Facility (ESRF) for the allocation of beamtime (beamline ID26).

[1] P. P. Feofilov, Photoexcited electron transfer in MeF_2-Eu, Sm single crystal, Opt. Spectrosk. **12**, 296 (1962).

[2] B. Welber, Reversible phototransfer of electrons between rare-earth ions in CaF_2, J. Chem. Phys. **42**, 4262 (1965).

[3] S. P. Keller, J. E. Mapes, and G. Cheroff, Studies on some infrared stimulable phosphors, Phys. Rev. **108**, 663 (1957).

[4] S. P. Keller and G. D. Pettit, Quenching, Stimulation, and exhaustion studies on some infrared stimulable phosphors, Phys. Rev. **111**, 1533 (1958).

[5] P. A. Jursinic, Characterization of optically stimulated luminescent dosimeters, OSLDs, for clinical dosimetric measurements, Med. Phys. **34**, 4594 (2007).

[6] E. G. Yukihara and S. W. S. McKeever, Optically stimulated luminescence (OSL) dosimetry in medicine, Phys. Med. Biol. **53**, R351 (2008).

[7] A. J. J. Bos, N. R. J. Poolton, J. Wallinga, A. Bessiere, and P. Dorenbos, Energy levels in $YPO_4 : Ce^{3+}$, Sm^{3+} studied by thermally and optically stimulated luminescence, Radiat. Meas. **45**, 343 (2010).

[8] A. J. J. Bos, Theory of thermoluminescence, Radiat. Meas. **41**, S45 (2006).

[9] K. Chakrabarti, V. K. Mathur, J. F. Rhodes, and R. J. Abbundi, Stimulated luminescence in rare-earth-doped MgS, J. Appl. Phys. **64**, 1363 (1988).

[10] K. Chakrabarti, V. K. Mathur, L. A. Thomas, and R. J. Abbundi, Charge trapping and mechanism of stimulated luminescence in CaS:Ce,Sm, J. Appl. Phys. **65**, 2021 (1989).

[11] D. Van der Heggen, D. R. Cooper, M. Tesson, J. J. Joos, J. Seuntjens, J. A. Capobianco, and P. F. Smet, Optically stimulated nanodosimeters with high storage capacity, Nanomaterials **9**, 1127 (2019).

[12] X. Ou, X. Qin, B. Huang, J. Zan, Q. Wu, Z. Hong, L. Xie, H. Bian, Z. Yi, X. Chen, Y. Wu, X. Song, J. Li, Q. Chen, H. Yang, and X. Liu, High-resolution x-ray luminescence extension imaging, Nature (London) **590**, 410 (2021).

[13] H. Nanto, Y. Hirai, M. Ikeda, M. Kadota, J. Nishishita, S. Nasu, and Y. Douguchi, A novel image storage sensor using photostimulated luminescence in SrS:Eu,Sm phosphor for electromagnetic waves such as x-rays, UV-rays and visible light, Sens. Actuators, A **53**, 223 (1996).

[14] P. K. Soltani, M. F. McAnally, and T. C. Chuang, System for reading a phosphor screen in filmless radiography, World Patent No. WO/1998/002780, 1996.

[15] P. Leblans, D. Vandenbroucke, and P. Willems, Storage phosphors for medical imaging, Materials **4**, 1034 (2011).

[16] T. Maldiney, A. Bessiere, J. Seguin, E. Teston, S. K. Sharma, B. Viana, A. J. J. Bos, P. Dorenbos, M. Bessodes, D. Gourier, D. Scherman, and C. Richard, The in vivo activation of persistent nanophosphors for optical imaging of vascularization, tumours and grafted cells, Nat. Mater. **13**, 418 (2014).

[17] D. C. Rodriguez Burbano, E. M. Rodriguez, P. Dorenbos, M. Bettinelli, and J. A. Capobianco, The near-IR photo-stimulated luminescence of $CaS:Eu^{2+}/Dy^{3+}$ nanophosphors, J. Mater. Chem. C **2**, 228 (2014).

[18] D. C. Rodriguez Burbano, S. K. Sharma, P. Dorenbos, B. Viana, and J. A. Capobianco, Persistent and photostimulated red emission in $CaS:Eu^{2+}$, Dy^{3+} nanophosphors, Adv. Opt. Mater. **3**, 551 (2015).

[19] C. Tydtgat, K. W. Meert, D. Poelman, and P. F. Smet, Optically stimulated detrapping during charging of persistent phosphors, Opt. Mater. Express **6**, 844 (2016).

[20] D. Van der Heggen, J. J. Joos, and P. F. Smet, Importance of evaluating the intensity dependency of the quantum efficiency: Impact on LEDs and persistent phosphors, ACS Photonics **5**, 4529 (2018).

[21] Y. H. Kim, P. Arunkumar, B. Y. Kim, S. Unithrattil, E. Kim, S. H. Moon, J. Y. Hyun, K. H. Kim, D. Lee, J. S. Lee, and W. B. Im, A zero-thermal-quenching phosphor, Nat. Mater. **16**, 543 (2017).

[22] R. E. Rojas-Hernandez, F. Rubio-Marcos, M. Á. Rodriguez, and F. Fernandez, Long lasting phosphors: $SrAl_2O_4$:Eu, Dy as the most studied material, Renewable Sustainable Energy Rev. **81**, 2759 (2018).

[23] M. Suta, F. Lavoie-Cardinal, and C. Wickleder, Underestimated color centers: Defects as useful reducing agents in lanthanide-activated luminescent materials, Angew. Chem., Int. Ed. **59**, 10949 (2020).

[24] J. J. Joos, D. Van der Heggen, L. Martin, L. Amidani, P. F. Smet, Z. Barandiarán, and L. Seijo, Broadband infrared LEDs based on europium-to-terbium charge transfer luminescence, Nat. Commun. **11**, 3647 (2020).

[25] Q. S. Chen, J. Wu, X. Y. Ou, B. L. Huang, J. Almutlaq, A. A. Zhumekenov, X. W. Guan, S. Y. Han, L. L. Liang, Z. G. Yi *et al.*, All-inorganic perovskite nanocrystal scintillators, Nature (London) **561**, 88 (2018).

[26] J. J. Joos, L. Seijo, and Z. Barandiarán, Direct evidence of intervalence charge-transfer states of Eu-doped luminescent materials, J. Phys. Chem. Lett. **10**, 1581 (2019).

[27] C. Linderälv, D. Åberg, and P. Erhart, Luminescence quenching via deep defect states: A recombination pathway via oxygen vacancies in Ce-doped YAG, Chem. Mater. **33**, 73 (2021).

[28] M. A. van de Haar, M. Tachikirt, A. C. Berends, M. R. Krames, A. Meijerink, and F. T. Rabouw, Saturation mechanisms in common LED phosphors, ACS Photonics **8**, 1784 (2021).

[29] P. Zheng, S. Li, T. Takeda, J. Xu, K. Takahashi, R. Tian, R. Wei, L. Wang, T.-L. Zhou, N. Hirosaki, and R.-J. Xie, Unraveling the luminescence quenching of phosphors under high-power-density excitation, Acta Mater. **209**, 116813 (2021).

[30] J. J. Joos, I Neefjes, L. Seijo, and Z. Barandiarán, Charge transfer from Eu^{2+} to trivalent lanthanide codopants: Systematic behavior across the series, J. Chem. Phys. **154**, 064704 (2021).

[31] Y. Tamura and A. Shibukawa, Optical studies of CaS:Eu, Sm infrared stimulable phosphors, Jpn. J. Appl. Phys. **32**, 3187 (1993).

[32] P. Dorenbos, Mechanism of persistent luminescence in Eu^{2+} and Dy^{3+} codoped aluminate and silicate compounds, J. Electrochem. Soc. **152**, H107 (2005).

[33] P. Dorenbos, A. J. J. Bos, and N. R. J. Poolton, Carrier recombination processes and divalent lanthanide spectroscopy in $YPO_4:Ce^{3+};L^{3+}$ (L = Sm,Dy,Tm), Phys. Rev. B **82**, 195127 (2010).

[34] J. Ueda, A. Meijerink, P. Dorenbos, A. J. J. Bos, and S. Tanabe, Thermal ionization and thermally activated crossover quenching processes for $5d$-$4f$ luminescence in $Y_3Al_{5-x}Ga_xO_{12} : Pr^{3+}$, Phys. Rev. B **95**, 014303 (2017).

[35] E. A. Radzhabov and V. A. Kozlovsky, Electron transfer between heterogeneous lanthanides in BaF_2 crystals, Radiat. Meas. **122**, 63 (2019).

[36] R. D. Shannon, Revised effective ionic-radii and systematic studies of interatomic distances in halides and chalcogenides, Acta Crystallogr., Sect A: Found. Adv. **32**, 751 (1976).

[37] Z. Barandiarán and L. Seijo, Intervalence charge transfer luminescence: Interplay between anomalous and $5d$-$4f$ emissions in Yb-doped fluorite-type crystals, J. Chem. Phys. **141**, 234704 (2014).

[38] L. Seijo and Z. Barandiarán, Intervalence charge transfer luminescence: The anomalous luminescence of cerium-doped $Cs_2LiLuCl_6$ elpasolite, J. Chem. Phys. **141**, 214706 (2014).

[39] Z. Barandiarán and L. Seijo, Metal-to-metal charge transfer between dopant and host ions: Photoconductivity of Yb-doped CaF_2 and SrF_2 crystals, J. Chem. Phys. **143**, 144702 (2015).

[40] Z. Barandiarán, A. Meijerink, and L. Seijo, Configuration coordinate energy level diagrams of intervalence and metal-to-metal charge transfer states of dopant pairs in solids, Phys. Chem. Chem. Phys. **17**, 19874 (2015).

[41] P. P. Ewald, Die berechnung optischer und elektrostatischer gitterpotentiale, Ann. Phys. (Berlin, Ger.) **369**, 253 (1921).

[42] N. S. Hush, Homogeneous and heterogeneous optical and thermal electron transfer, Electrochim. Acta **13**, 1005 (1968).

[43] M. Douglas and N. M. Kroll, Quantum electrodynamical corrections to the fine structure of helium, Ann. Phys. (NY) **82**, 89 (1974).

[44] B. O. Roos, P. R. Taylor, and P. E. M. Siegbahn, A complete active space SCF method (CASSCF) using a density-matrix formulated super-CI approach, Chem. Phys. **48**, 157 (1980).

[45] P. E. M. Siegbahn, A. Heiberg, B. O. Roos, and B. Levy, Comparison of the super-CI and the Newton-Raphson scheme in the complete active space SCF method, Phys. Scr. **21**, 323 (1980).

[46] P. E. M. Siegbahn, A. Heiberg, J. Almlöf, and B. O. Roos, The complete active space SCF (CASSCF) method in a Newton-Raphson formulation with application to the HNO molecule, J. Chem. Phys. **74**, 2384 (1981).

[47] B. A. Hess, Relativistic electronic-structure calculations employing a two-component no-pair formalism with external-field projection operators, Phys. Rev. A **33**, 3742 (1986).

[48] Z. Barandiarán and L. Seijo, The ab ianitio model potential representation of the crystalline environment. Theoretical study of the local distortion on NaCl:Cu^+, J. Chem. Phys. **89**, 5739 (1988).

[49] J. Olsen, B. O. Roos, P. Jørgensen, and H. J. A. Jensen, Determinant based configuration-interaction algorithms for complete and restricted configuration-interaction spaces, J. Chem. Phys. **89**, 2185 (1988).

[50] P.-Å. Malmqvist, A. Rendell, and B. O. Roos, The restricted active space self-consistent-field method, implemented with a split graph unitary-group approach, J. Phys. Chem. **94**, 5477 (1990).

[51] K. Andersson, P.-Å. Malmqvist, B. O. Roos, A. J. Sadlej, and K. Wolinski, Second-order perturbation theory with a CASSCF reference function, J. Phys. Chem. **94**, 5483 (1990).

[52] L. Seijo and Z. Barandiarán, Ab initio model potential study of local distortions around Cr^+ and Cr^{3+}, J. Chem. Phys. **94**, 8158 (1991).

[53] K. Andersson, P.-Å. Malmqvist, and B. O. Roos, Second-order perturbation theory with a complete active space self-consistent field reference function, J. Chem. Phys. **96**, 1218 (1992).

[54] A. Zaitsevskii and J.-P. Malrieu, Multi-partitioning quasidegenerate perturbation theory. A new approach to multireference Møller-Plesset perturbation theory, Chem. Phys. Lett. **233**, 597 (1995).

[55] R. Llusar, M. Casarrubios, Z. Barandiarán, and L. Seijo, *Ab initio* model potential calculations on the electronic spectrum of Ni^{2+}-doped MgO including correlation, spin-orbit and embedding effects, J. Chem. Phys. **105**, 5321 (1996).

[56] B. A. Hess, C. M. Marian, U. Wahlgren, and O. Gropen, A mean-field spin-orbit method applicable to correlated wavefunctions, Chem. Phys. Lett. **251**, 365 (1996).

[57] N. Forsberg and P.-Å. Malmqvist, Multiconfiguration perturbation theory with imaginary level shift, Chem. Phys. Lett. **274**, 196 (1997).

[58] J. Finley, P.-Å. Malmqvist, B. O. Roos, and L. Serrano-Andrés, The multi-state CASPT2 method, Chem. Phys. Lett. **288**, 299 (1998).

[59] J.-P. Launay, Long-distance intervalence electron transfer, Chem. Soc. Rev. **30**, 386 (2001).

[60] P.-Å. Malmqvist, B. O. Roos, and B. Schimmelpfennig, The RASSI approach with spin-orbit coupling, Chem. Phys. Lett. **357**, 230 (2002).

[61] J. Paulovic, T. Nakajima, K. Hirao, R. Lindh, and P.-Å. Malmqvist, Relativistic and correlated calculations on the ground and excited states of ThO, J. Chem. Phys. **119**, 798 (2003).

[62] G. Karlström, R. Lindh, P.-Å. Malmqvist, B. O. Roos, U. Ryde, V. Veryazov, P. O. Widmark, M. Cossi, B. Schimmelpfennig, P. Neogrady, and L. Seijo, MOLCAS: A program package for computational chemistry, Comput. Mater. Sci. **28**, 222 (2003).

[63] B. O. Roos, R. Lindh, P. Å. Malmqvist, V. Veryazov, and P. O. Widmark, Main group atoms and dimers studied with a new relativistic ANO basis set, J. Phys. Chem. A **108**, 2851 (2004).

[64] G. Ghigo, B. O. Roos, and P.-Å. Malmqvist, A modified definition of the zeroth-order Hamiltonian in multiconfigurational perturbation theory (CASPT2), Chem. Phys. Lett. **396**, 142 (2004).

[65] P.-Å. Malmqvist, K. Pierloot, A. R. M. Shahi, C. J. Cramer, and L. Gagliardi, The restricted active space followed by second-order perturbation theory method: Theory and application to the study of CuO_2 and Cu_2O_2 systems, J. Chem. Phys. **128**, 204109 (2008).

[66] A. Gellé and M. B. Lepetit, Fast calculation of the electrostatic potential in ionic crystals by direct summation method, J. Chem. Phys. **128**, 244716 (2008).

[67] B. O. Roos, R. Lindh, P. Å. Malmqvist, V. Veryazov, P. O. Widmark, and A. C. Borin, New relativistic atomic natural orbital basis sets for lanthanide atoms with applications to the Ce diatom and LuF_3, J. Phys. Chem. A **112**, 11431 (2008).

[68] Z. Barandiarán and L. Seijo, Radial correlation effects on interconfigurational excitations at the end of the lanthanide series: A restricted active space second order perturbation study of Yb^{2+} and $SrCl_2$:Yb^{2+}, J. Chem. Phys. **138**, 074102 (2013).

[69] J. J. Joos, P. F. Smet, L. Seijo, and Z. Barandiarán, Insights into the complexity of the excited states of Eu-doped luminescent materials, Inorg. Chem. Front. **7**, 871 (2020).

[70] See Supplemental Material at http://link.aps.org/supplemental/10.1103/PhysRevB.104.L201108 for technical details of the used theoretical and experimental methods, as well as intermediate results.

[71] Y. R. Shen, K. L. Bray, and W. B. Holzapfel, Effect of temperature and pressure on radiative and nonradiative transitions of Sm^{2+} in SrFCl, J. Lumin. **72-74**, 266 (1997).

[72] C. Wickleder, Excited states of Sm^{2+} in chloride host lattices, J. Lumin. **94-95**, 127 (2001).

[73] M. Suta and C. Wickleder, Synthesis, spectroscopic properties and applications of divalent lanthanides apart from Eu^{2+}, J. Lumin. **210**, 210 (2019).

[74] D. L. Wood and W. Kaiser, Absorption and fluorescence of Sm^{2+} in CaF_2, SrF_2, and BaF_2, Phys. Rev. **126**, 2079 (1962).

[75] E. Loh, $4f^n \rightarrow 4f^{n-1}5d$ spectra of rare-earth ions in crystals, Phys. Rev. **175**, 533 (1968).

[76] G. H. Dieke, H. M. Crosswhite, and B. Dunn, Emission spectra of the doubly and triply ionized rare earths, J. Opt. Soc. Am. **51**, 820 (1961).

[77] G. H. Dieke and H. M. Crosswhite, The spectra of the doubly and triply ionized rare earths, Appl. Opt. **2**, 675 (1963).

[78] E. J. Heller, Time-dependent approach to semiclassical dynamics, J. Chem. Phys. **62**, 1544 (1975).

[79] E. J. Heller, The semiclassical way to molecular spectroscopy, Acc. Chem. Res. **14**, 368 (1981).

[80] R. H. Packwood and J. D. Brown, A Gaussian expression to describe $\phi(\rho z)$ curves for quantitative electron probe microanalysis, X-Ray Spectrom. **10**, 138 (1981).

[81] C. Gauthier, V. A. Sole, R. Signorato, J. Goulon, and E. Moguiline, The ESRF Beamline ID26: X-ray absorption on ultra dilute sample, J. Synchrotron Radiat. **6**, 164 (1999).

[82] P. Glatzel, T. C. Weng, K. Kvashnina, J. Swarbrick, M. Sikora, E. Gallo, N. Smolentsev, and R. A. Mori, Reflections on hard x-ray photon-in/photon-out spectroscopy for electronic structure studies, J. Electron Spectrosc. **188**, 17 (2013).

[83] J. A. van Bokhoven and C. Lamberti, *X-Ray Absorption and X-Ray Emission Spectroscopy: Theory and Applications* (Wiley, New York, 2016), Vol. 1.

[84] Z. Hu, G. Kaindll, and G. Meyer, X-ray absorption near-edge structure at the L_{I-III} thresholds of Pr, Nd, Sm, and Dy compounds with unusual valences, J. Alloys Compd. **246**, 186 (1997).

[85] J. J. Joos, K. Korthout, L. Amidani, P. Glatzel, D. Poelman, and P. F. Smet, Identification of Dy^{3+}/Dy^{2+} as Electron Trap in Persistent Phosphors, Phys. Rev. Lett. **125**, 033001 (2020).